Thermally Stable Plasmonic Nanocermets Grown on Microengineered Surfaces as Versatile Surface Enhanced Raman Spectroscopy Sensors for Multianalyte Detection

Nitant Gupta,[†] Disha Gupta,[†] Shantanu Aggarwal,[‡] Soumik Siddhanta,[‡] Chandrabhas Narayana,[‡] and Harish C. Barshilia*[,†]

[†]Nanomaterials Research Laboratory, Surface Engineering Division, CSIR−National Aerospace Laboratories, Bangalore 560 017, India

[‡]Light Scattering Laboratory, Chemistry and Physics of Materials Unit, Jawaharlal Nehru Centre for Advanced Scientific Research, Bangalore 560 064, India

Ⓢ *Supporting Information*

ABSTRACT: Noble metal nanoparticle-based plasmonic sensors, fabricated by top-down and colloidal routes, are widely used for high sensitivity detection of diverse analyte molecules using surface enhanced Raman spectroscopy (SERS). However, most of these sensors do not show stability under harsh environments, which limits their use as versatile SERS substrates. In this work, we report the first use of plasmonic nanocermets, grown on microengineered Si surfaces, as potential candidates for a highly robust SERS sensor. The robustness of the sensor is attributed to the anchoring of the nanoparticles in the nanocermet, which is an

important factor for exploiting its reusability. The fairly uniform distribution of nanoparticles in the sensor led to high enhancement factors (10^6−10^7) and enabled the detection of low concentrations of a wide range of analytes, including differently charged biomolecules, which is extremely difficult for other SERS sensors. With more precise control over the particle geometry and distribution, plasmonic nanocermets may play an important role in ultrasensitive SERS measurements in adverse conditions such as high temperature.

KEYWORDS: plasmonic nanocermets, surface enhanced Raman spectroscopy, Ag nanoparticles, high thermal stability, biomolecule detection
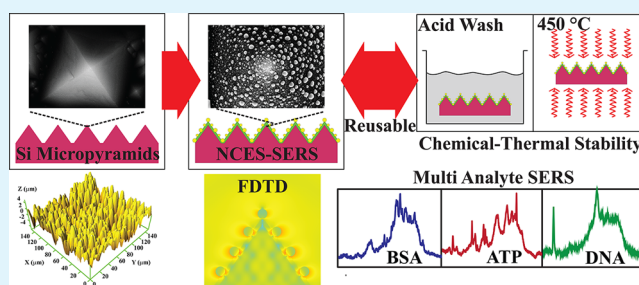
■ INTRODUCTION

A nanocermet is a nanoscale composite of a ceramic ("cer") material, which is present in the matrix phase, and a metal ("met"), which is present in the form of nanoparticles (NPs). Plasmonic nanocermets use noble metal NPs (Au, Ag, Cu) as they show strong absorption of the electromagnetic radiation (typically in the UV−vis−NIR spectral ranges) due to the phenomenon of localized surface plasmon resonance (LSPR).[1,2] The resonance behavior of plasmonic nanocermets is greatly affected by the geometry (size and shape) and the distribution of the NPs (interparticle spacing) and the dielectric properties of the ceramic material. In past and recent literature, many instances of nanophotonic devices have employed the use of plasmonic nanocermet thin films in relation to photothermal conversion, optical waveguiding, and photochromic and photoelectrochemical applications, among others.[3,4]

An important application of the LSPR phenomenon is used in surface enhanced Raman spectroscopy (SERS), to provide very high electric field intensities in the vicinity of NPs (high near-field intensities) for the detection of various analytes.[5−10] The plasmonic properties of noble metal NPs, in the form of

solid sensors, where NPs are assembled or deposited on plane or micro-/nanoengineered surfaces, or as liquid sensors using colloidal suspensions of NPs, have been widely studied for high enhancement of SERS signal.[11−25] However, for the case of solid sensors, highly ordered arrangement of metal NPs is essential to ensure strong plasmonic coupling. This is often achieved through the use of advanced fabrication techniques (e-beam lithography, focused ion beam, etc.) which requires a high level of sophistication and has low time-and-cost effectiveness and limited spatial resolution due to the electron/ion-beam size.[9,26]

For the case of liquid SERS sensors, colloidal suspensions of NPs have a tendency to nonuniformly agglomerate in the presence of salts and some analytes, thereby giving non-reproducible enhancements.[23,25] Therefore, capping agents are added to colloidal suspensions for the stabilization of NPs, which greatly affect their SERS performance for two main

reasons.[6,27−29] First, the capping agent acts as an impediment for the analyte molecule to directly interact with the NP. As most of the capping agents are ionically charged, they repel similarly charged analyte molecules, thus limiting their range of use.[6] Second, the nonreplaceable nature of the capping agent makes liquid SERS sensor difficult to regenerate and, hence, are nonreusable.[6] In addition to the above-mentioned drawbacks of the solid and liquid SERS sensors, they are also unstable at high temperatures due to oxidation of NPs and are susceptible to degradation when exposed to harsh chemical environments.

Considering these shortcomings, we present a simple approach to design a SERS sensor, which combines the outstanding properties of nanocermets with light trapping property of microengineered Si surface.[1,2,30] This was achieved by uniformly dispersing silver NPs (AgNPs) in an amorphous silicon nitride (a-Si$_3$N$_4$) matrix, which protects the AgNPs from degradation.[31] Si (100) wafers were anisotropically etched to obtain the micropyramidal structure,[30,32] which contribute to the enhanced nucleation and growth of AgNPs in addition to the light trapping effect.[33] Hence, the resulting nanocermet-on-etched-Si-based-SERS sensor (hereafter called NCES-SERS sensor), exhibited multifunctional characteristics such as reusability, high temperature stability, chemical stability, and detection of various analytes at very low concentrations. The uniformity in the microstructure, as well as, in the distribution of the AgNPs resulted in high enhancement factors (10^6–10^7). The presence of a-Si$_3$N$_4$ matrix stabilizes the distribution of NPs by anchoring them to the surface of the micropyramids.

In comparison, a roughened Ag substrate, which has been conventionally used for SERS applications, has scarce and nonhomogeneous distribution of hot-spots.[34] This makes their SERS signals nonreproducible. In some cases of mechanically roughened Ag surfaces,[35] the enhancement factor has been shown to be as low as 10^3, which is much lower than what we found for our NCES-SERS sensor. Moreover, due to the flat morphology of the roughened Ag substrate, there would be an absence of interesting optical effects like multiple reflections, which can help in further enhancement, as observed due to the pyramidal morphology of our sensors. Therefore, we believe that gaining control over the NP localization on the substrate, and the substrate morphology is critical for higher enhancement factors, and also for obtaining reproducible SERS signals.

The potential of our NCES-SERS sensor for multidisciplinary applications will be substantiated with experimental results. We believe that our sensor can be employed in the fields of biomedicine, pharmacology, microbiology, forensics, chemistry, environmental sciences, etc. Given the fact that both the etching of Si, as well as the sputter deposition of nanocermets, are well-established techniques in the semiconductor industry, the proof-of-concept of the present work can be easily upscaled. Additionally, there is a demand for new techniques which use nonlabeled methods (such as SERS) to avoid the use of radio labeling or fluorescence tagging.[36] Our NCES-SERS sensor provides a cost-effective and viable alternative to these methods.

■ EXPERIMENTAL SECTION

Anisotropic Etching of Silicon. A solution of 10% potassium hydroxide (KOH) and 20% ethylene glycol (HO−CH$_2$−CH$_2$−OH) was used to etch Si (100) wafers at a bath temperature of 85 °C;[32] the details of which are provided in Supporting Figure S1.

Growth of the Ag:a-Si$_3$N$_4$ Nanocermet Thin Film on Anisotropically Etched Si. Ag:a-Si$_3$N$_4$ nanocermet thin films were grown on anisotropically etched Si substrates using a reactive direct current unbalanced magnetron sputtering system. High purity targets of Ag (99.99%) and Si$_3$N$_4$ (99.99%) with diameter 0.075 m were used for deposition of the nanocermet. Before the deposition process, the vacuum chamber was pumped down to a base pressure of 5.5×10^{-4} Pa. During deposition, the substrate temperature was maintained at 150 °C, the Ar gas flow rate at 30 SCCM and the operating pressure at 3.4 Pa. An asymmetric bipolar pulsed DC generator (f = 100 kHz, pulse width = 2976 ns, positive pulsed bias = +37 V) was used to sputter the Ag target while an RF power supply (f = 13.56 MHz) was used to sputter the Si$_3$N$_4$ target. In the beginning of the deposition process, sputtering was carried out at P_{Ag} of 20 W to deposit ~10 nm thick Ag metal interlayer. Afterward, Ag:a-Si$_3$N$_4$ nanocermet layer was deposited by cosputtering of Ag and Si$_3$N$_4$ targets. The power of Si$_3$N$_4$ target was kept constant at 325 W, whereas P_{Ag} was varied from 12 to 18 W to obtain different Ag contents in the nanocermet thin films. During the deposition the sample holder was rotated uniformly to achieve highly uniform thin films. After deposition the samples were annealed in air for 1 h at 500 °C. The samples were allowed to cool down under ambient conditions.

Characterization of NCES-SERS Sensor. The surface morphology and microstructure were analyzed using field emission scanning electron microscopy (FESEM, Supra 40VP, Carl Zeiss) and 3D surface profilometer (Nanomap). The structural and chemical characterization of the sensor was carried out using X-ray diffraction (XRD, Bruker D8) in thin film mode and X-ray photoelectron spectroscopy (XPS, SPECS). The plasmonic behavior of the sensor was studied using a UV−vis spectrophotometer (PerkinElmer, Lambda 750).

SERS Measurements. 180° backscattering geometry was used to record Raman and SERS spectra. The excitation source was 532 nm from a diode pumped frequency doubled Nd:YAG solid state laser (Photop Suwtech Inc., GDLM-5015 L). The numerical aperture of the lens was 0.45 with a working distance of 17 mm. A custom built Raman spectrometer equipped with a SPEX TRIAX 550 monochromator and a liquid nitrogen cooled CCD were used to record the spectra. Laser power at the sensor was 8 mW without filters, and appropriate neutral density filters were used to control the laser power at the sensor. The typical acquisition time was 10−30 s. For obtaining SERS spectra, 10 μL of the analyte solution was dropped on the sensor and allowed to dry. SERS spectra were then collected from three different locations and averaged.

In order to study the thermal stability of the sensor, after acquiring the SERS spectra of a given analyte, it was removed by heating the sensor at 450 °C for 15 min (with a heating rate of 10 °C/min). This procedure was repeated 5 times to demonstrate the reusability of the substrate. Similarly, for chemical stability, the sensor was dipped in concentrated HCl solution for 5 min and then washed thoroughly with ethanol. Analyte solution was then added to obtain the SERS spectra of the next cycle.

Finite Difference Time Domain (FDTD) Simulations of NCES-SERS Sensor Process Parameters. All the FDTD simulations were performed using Lumerical FDTD Solutions (Trial License). All the data generated from the simulation were plotted in MATLAB. The micropyramids were represented by triangles with base length P, NPs as circles with diameter d, and edge-to-edge NP spacing S. The thickness of dielectric material was $0.7d$, wherein the NPs were embedded to a depth of $0.2d$. A 10 nm interlayer of Ag was also used in the model. The left and right boundaries of the simulation region were assigned periodic boundary conditions (PBC) (periodicity = P), while the top and bottom boundaries were modeled with perfectly matched layers (PML). Mesh size for the simulation was taken as 2 nm (in both X- and Y- directions) due to computational limitations. A p-polarized light source was introduced at the top with λ = 532 nm.

■ RESULTS AND DISCUSSION

We begin by discussing the characterization of the NCES-SERS sensor. The anisotropic etching of Si (100) wafer (described in Supporting Figure S1) results in the formation of micropyramids with base widths in the range of 1−10 μm.[30] Figure
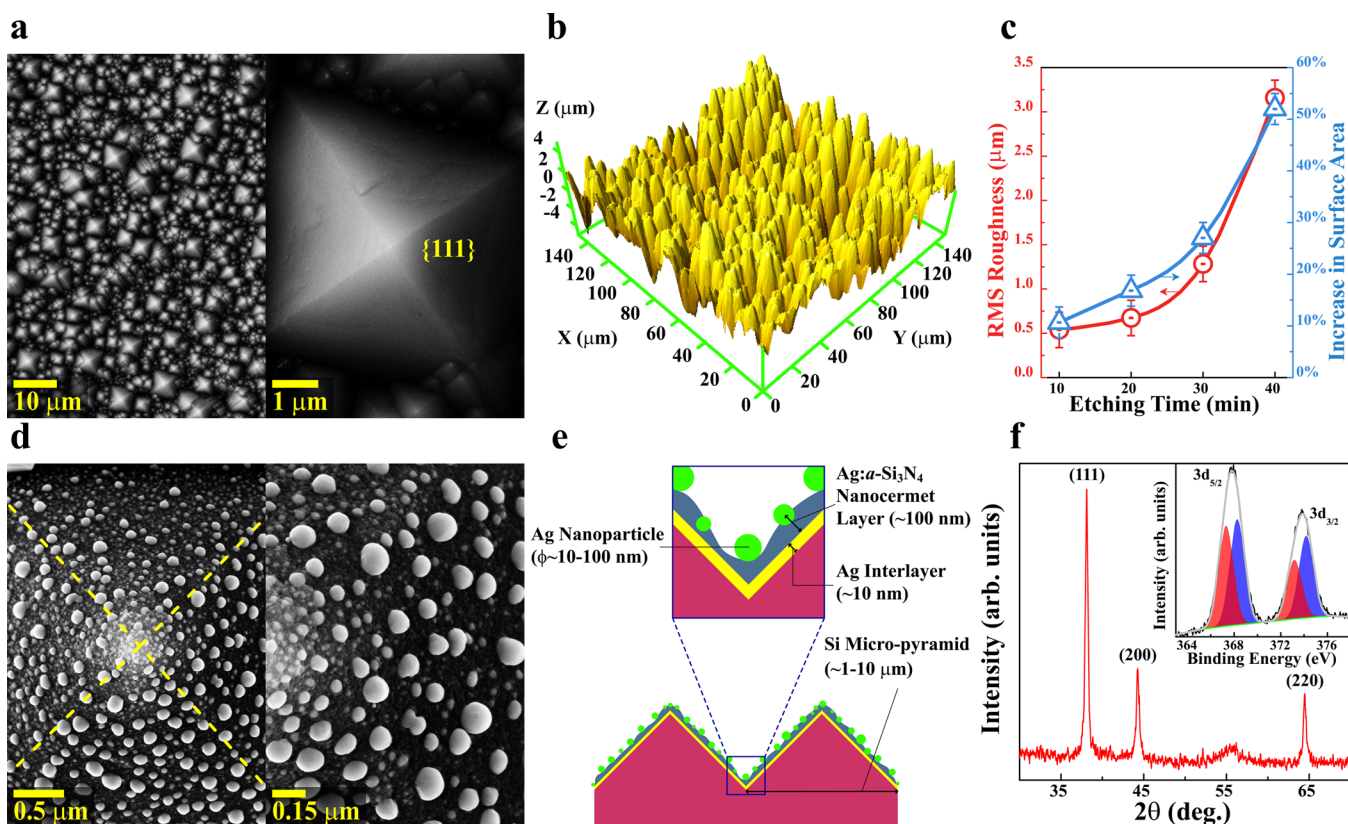
Figure 1. Characterization of NCES-SERS sensor. (a) Low (left) and high (right) magnification FESEM micrographs for the anisotropically etched Si (100) wafer. The scale bars for the left and right images are of lengths, 10 and 1 μm, respectively. (b) 3D surface roughness profile of an etched Si substrate. (c) Plot of etching time with RMS roughness (left) and the increase in surface area (right). (d) Low (left) and high (right) magnification FESEM micrographs for the NCES-SERS sensor. The scale bars for the left and right images are of lengths, 0.5 and 0.15 μm, respectively. (e) Schematic representation of the NCES-SERS sensor. (f) XRD pattern of the nanocermet thin film with the crystal planes of Ag marked. The inset shows the XPS spectrum of Ag $3d_{5/2}$ and $3d_{3/2}$ transitions and the red shaded peaks correspond to AgO, while blue shaded peaks correspond to Ag.
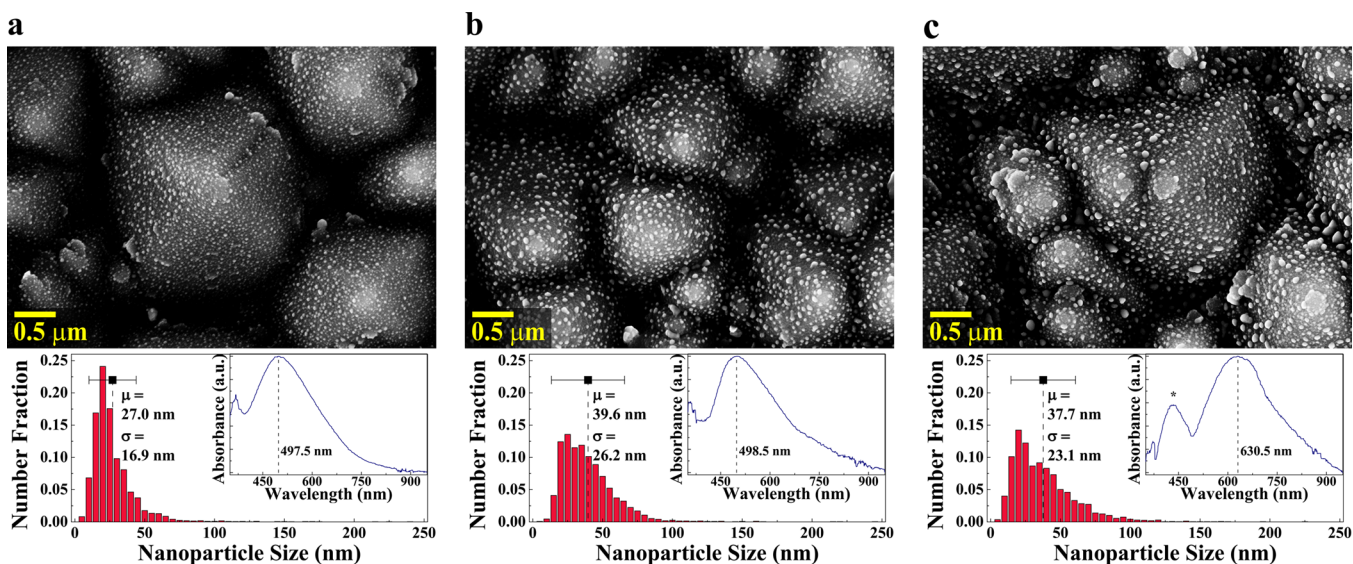

Figure 2. Dependence of surface plasmon resonance on the NP size and distribution. FESEM micrographs (scale bar = 0.5 μm), NP size distribution histograms and the UV−vis absorbance plots (inset) for the NCES-SERS sensors at RMS surface roughness, R_{RMS} = 0.63 μm but different Ag target power levels: P_{Ag} = (a) 12, (b) 14, and (c) 16 W. μ and σ represent the mean and standard deviation of the histograms, respectively.

1a gives the FESEM micrographs of the micropyramidal morphology that is seen in these cases. The presence of these micropyramids is responsible for imparting the microscale roughness, which affects the nucleation, growth, and distribu-

tion of the AgNPs.[33] The pyramidal microstructure results in the formation of valleys which lead to several interesting microstructural and optical properties as presented in Supporting Figure S2−S5.[30] A representative 3D surface profile
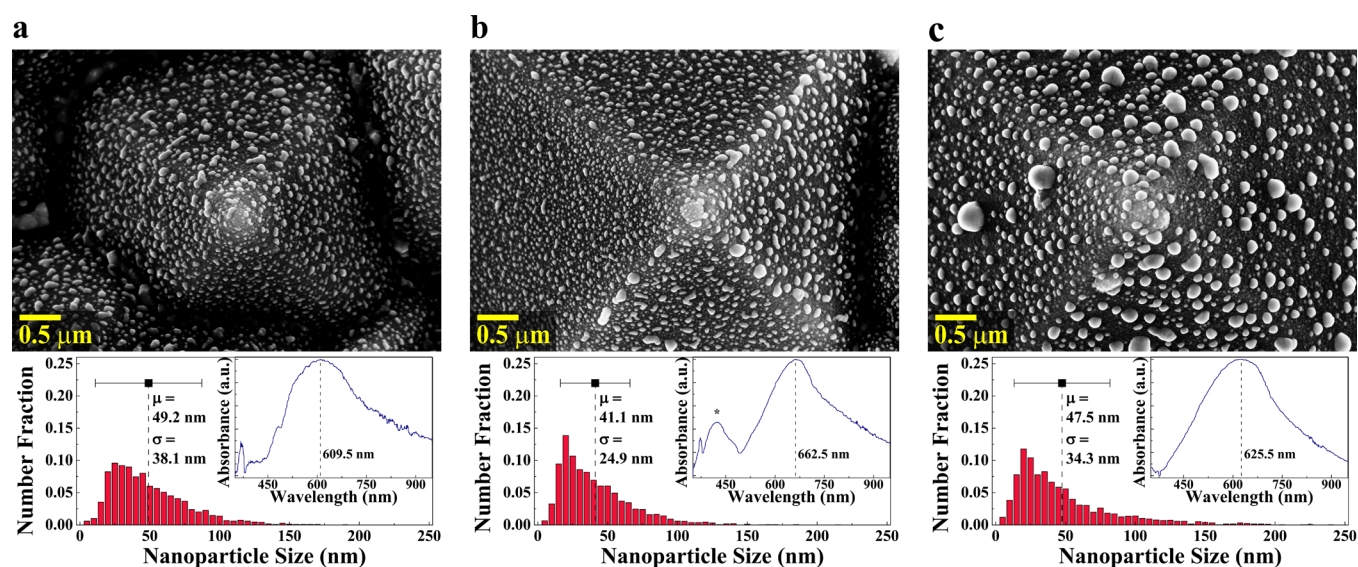
Figure 3. FESEM micrographs, NP size distribution histograms, and the UV−vis absorbance plots (inset) for the NCES-SERS sensors at Ag target power, P_{Ag} = 18 W but different RMS surface roughness: R_{RMS} = (a) 0.54, (b) 1.28, and (c) 3.15 μm. μ and σ represent the mean and standard deviation of the histograms, respectively.

for the etched Si surface is shown in Figure 1b, which clearly indicates that the average height of the micropyramids is uniformly distributed throughout the surface. The root-mean-square roughness (R_{RMS}) for these samples was in the range of 0.54−3.15 μm and was controlled by changing the duration of etching. Figure 1c shows a plot between R_{RMS} and the duration of the anisotropic etching along with the corresponding increase in the surface area. Figure 1d shows the FESEM micrograph of NCES-SERS sensor at high magnification. The edges of the Si micropyramid beneath the nanocermet thin film are depicted by dashed lines. The nanocermet film comprises of the AgNPs dispersed in a-Si_3N_4 matrix. The average NP size was found to change with the power that was applied to the Ag target (P_{Ag}) during deposition as well as R_{RMS} of the Si substrate. The NP sizes were in the range of 10−100 nm. The schematic in Figure 1e gives a representation of the NCES-SERS sensor. An interlayer of Ag (10 nm) was deposited on the etched Si surface to provide more opportunities for multiple reflections and to reduce any absorption in the underlying Si substrate. To verify the presence of AgNPs in the nanocermet thin film, the XRD plot in Figure 1f shows the characteristic crystal planes of the polycrystalline Ag. Si_3N_4 peaks were not detected in the XRD data, confirming its amorphous nature. Since the samples were heated in air at 500 °C for 1 h, surface oxidation of AgNPs is expected, which was confirmed by XPS.[37,38] The core-level spectrum of Ag is provided as an inset in Figure 1f. The presence of AgO and Ag was confirmed by deconvolution of the peaks. The peaks shaded in red (367.3 and 373.2 eV) belong to AgO, while the peaks shaded in blue (368.3 and 374.2 eV) belong to Ag. The detailed analysis of the core level XPS O 1s spectrum is given in Supporting Figure S6. Based upon these analyses it can be concluded that the majority of Ag was in the metallic state as no oxide peaks were noticeable in the XRD data.

Figures 2 and 3 show the variations in the AgNP size distribution (as per procedure outlined in Supporting Figure S7) with P_{Ag} (Figure 2a−c) and R_{RMS} of the etched Si (Figure 3a−c), respectively. The corresponding UV−vis spectra are provided as insets. There is a direct correlation between the NP

size distribution and the UV−vis spectra. The different NP sizes give rise to different dipole plasmon modes. The dipole plasmon mode red-shifted with an increase in P_{Ag} as the average size of the AgNPs increased.[10,39] The pyramid size has no significant role on the size of the AgNPs as no major shift in the dipole plasmon peak could be observed. The distribution of the AgNPs was found to vary with different etched planes, presumably because of the shadowing effect in the sputtering process.[40] As a consequence of this, two major size distributions can be observed very clearly in Figure 3b. This distribution leads to an additional dipole plasmon mode (or quadrupole plasmon mode) at lower wavelengths in the UV−vis spectra, marked with "*". Larger NPs often give rise to plasmon bands which are red-shifted due to electromagnetic retardation effect.[41,42] It is to be noted that the presence of a-Si_3N_4 matrix plays a crucial role in anchoring the AgNPs to the Si micropyramids, which do not agglomerate/aggregate or roll down even after annealing up to 500 °C in air (as shown in Supporting Figure S5).

The process parameters used to fabricate NCES-SERS sensor influenced the SERS signal of thiophenol (C_6H_6S or PhSH), which was used as a model analyte for SERS enhancement factor (G) calculations,[43] the details of which are provided in the Supporting Information. The variations in the SERS signal intensity of PhSH can be observed in Figure 4. Inhomogeneous broadening of Raman peaks (or the differences in their relative scaling) was observed due to the "many molecule" SERS effect.[44] The enhancement of a particular mode depends on the orientation of the polarizability component with respect to the NP surface (maximum when perpendicular).[45] It must be noted that the surface of our NCES-SERS sensor was fairly homogeneous, in terms of its AgNP distribution, and displayed similar SERS spectra at randomly selected locations (Supporting Figure S8).

The enhancement factor for our NCES-SERS sensor was in the range of 10^6−10^7 for PhSH (Figure 4). It has been reported that $G > 10^8$ could be achieved using Ag based nanostructures, which are highly aggregated systems with nonuniform hot spots.[23,25] Our NCES-SERS sensor on the other hand consists

a

200 cps

$G = 9.19 \times 10^6$

18 W

$G = 5.36 \times 10^6$

16 W

$G = 3.22 \times 10^6$

14 W

$G = 1.99 \times 10^6$

12 W

Intensity (cps)

800   1100   1400   1700

Raman Shift (cm^{-1})

b

100 cps

$G = 3.87 \times 10^6$

100 nm

$G = 1.84 \times 10^6$

75 nm

$G = 1.51 \times 10^6$

50 nm

$G = 0.43 \times 10^6$

25 nm

Intensity (cps)

800   1100   1400   1700

Raman Shift (cm^{-1})

c

$G = 9.01 \times 10^6$

200 cps

3.00 μm

$G = 9.37 \times 10^6$

1.31 μm

$G = 9.19 \times 10^6$

0.67 μm

$G = 3.58 \times 10^6$

0.33 μm

Intensity (cps)

800   1100   1400   1700

Raman Shift (cm^{-1})

d

En. Factor ($\times 10^6$)

9
7
5
3
1

12   14   16   18

Ag Power (W)

En. Factor ($\times 10^6$)

9
7
5
3

0   1   2   3

RMS Roughness (μm)

En. Factor ($\times 10^6$)

4
3
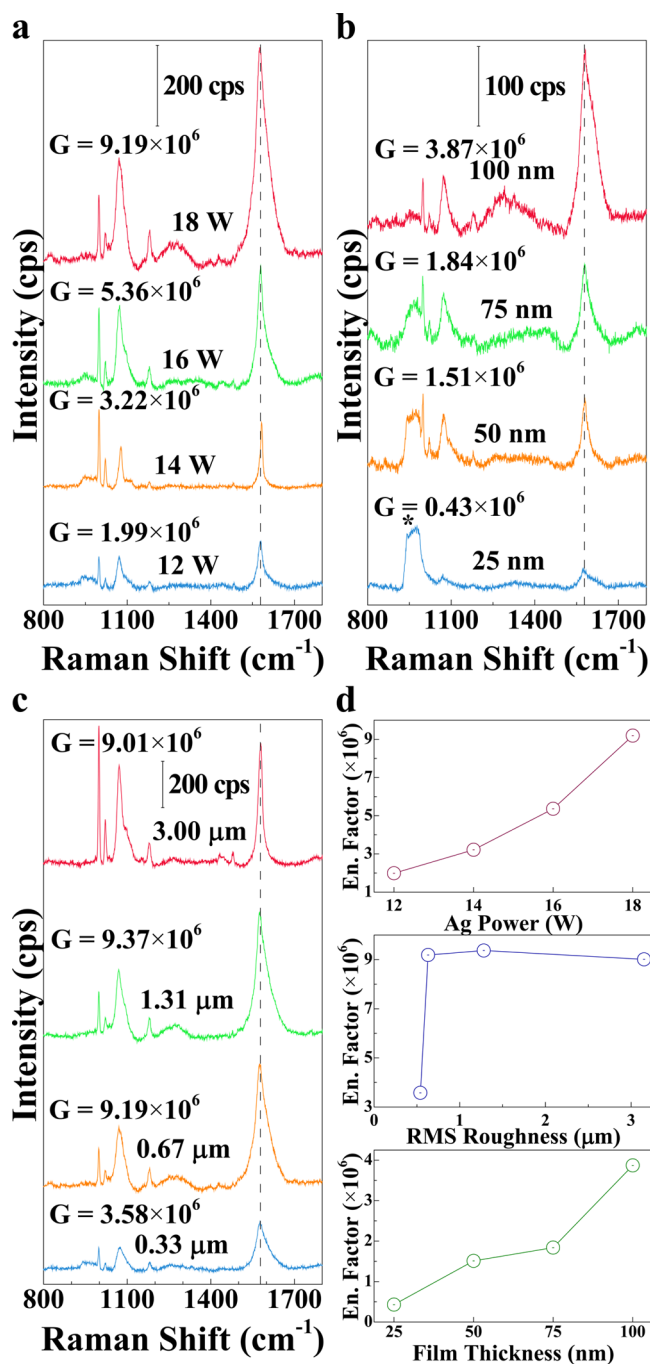2
1
0

25   50   75   100

Film Thickness (nm)

Figure 4. SERS spectra for the NCES-SERS sensors prepared by varying different experimental parameters: (a) Ag target power, (b) film thickness, and (c) RMS surface roughness. PhSH is used as a model analyte. (d) The variation in the SERS enhancement factors (written as En. Factor) for NCES-SERS sensors calculated from the SERS plots in parts a−c.

of fairly uniform distribution of AgNPs, that are anchored in a-Si_3N_4 matrix, without undergoing aggregation, which are important factors for chemical and thermal stability. The variations in the size and distribution of AgNPs, as shown in Figures 2 and 3, lead to changes in SERS enhancement factors. As the size of AgNPs increases with P_{Ag} and the film thickness (t_{film}), an increase in G is observed as depicted in Figure 4a and b. Since, there was no major change in the size and distribution of the AgNPs due to the changes in the pyramid size (in other

words, R_{RMS}), illustrated in Figure 3a−c, G is almost same after a critical R_{RMS} (Figure 4c). As also can be seen in Figure 4b, the presence of the second-order Raman signal of Si (marked with "*") decreases with an increase in t_{film}. From the above observations, P_{Ag} of 18 W, R_{RMS} of 1.33 μm, and t_{film} of 100 nm were found to be optimum conditions for maximum SERS signal enhancement in the present work. The variation in the SERS enhancement factors have also been plotted separately in Figure 4d to illuminate its dependence on the process parameters.

Since nanocermets are known to be stable at high temperature, it is possible to utilize them for high temperature SERS studies.[46] In the Supporting Figure S9, we have provided the temperature dependent SERS of PhSH up to 450 °C in air. Since the SERS at 450 °C has no observable peaks, resulting from the complete disintegration and evaporation of PhSH without affecting the sensor, we exploited it for the reusability of our NCES-SERS sensor as given in Figure 5a. It can be seen from the figure that after cyclic heating, the SERS intensity for PhSH remains almost constant. The NCES-SERS sensor subjected up to 5 cycles of annealing was further examined under FESEM and the corresponding micrograph is shown in Figure 5a (bottom), highlighting the anchoring effect of a-Si_3N_4 matrix. We also investigated the reusability of the NCES-SERS sensor through chemical treatment (HCl immersion), as given in Figure 5b. The Rhodamine 6G (R6G) dye molecule was used instead of PhSH, as it does not form a direct covalent bond with Ag, which can be removed easily by chemical wash. Interestingly, after the first cycle, an increase in the SERS signal was observed for R6G analyte, which might be due to the removal of native oxide layer on the AgNPs (Figure 1f).[38,37] However, the FESEM micrograph (Figure 5b, bottom) taken after three cycles indicate slight leaching and displacement of the AgNPs, which is expected to deteriorate after subsequent cycles, thus limiting its reusability through chemical route. Contrary to this, the reusability through heat treatment does not lead to any significant changes in the size and distribution of AgNPs. Therefore, the reusability through heat treatment is better than commonly used chemical treatment.[47]

To further demonstrate the versatility of our NCES-SERS sensor, different analytes of biological significance were used for SERS measurements as shown in Figure 6a. The detailed SERS peak assignments are provided in the Supporting Information (Tables S1−S6). Two important classes of biomolecules were investigated, namely proteins (lysozyme and bovine serum albumin, BSA) and nucleic acids (deoxyribonucleic acid, DNA). The SERS spectrum of adenosine triphosphate (ATP) was also studied, which is of common interest because of its central role in biological energy-transfer reactions.[20] We have used the NCES-SERS sensor to sense low concentration (10^{-8} M) of genomic DNA as well as molecular ATP and have obtained unique fingerprints of these molecules which might be used for multiplex detection.[48−50] The SERS spectra of two differently charged protein molecules, lysozyme (pI = 11.35), and BSA (pI = 4.9) could be detected by our NCES-SERS sensor (Figure 6a). This is not possible with conventional colloidal based SERS sensors due to the presence of charged capping agents.[6,27−29] Furthermore, the bare NP surface of our sensor does not form complexes with biomolecules (as delicate as proteins) due to its chemical stability, which is an important criterion for their detection. Additionally, our sensor can easily accommodate large sized biomolecules like proteins and DNA in the gaps between AgNPs, which exposes more molecular
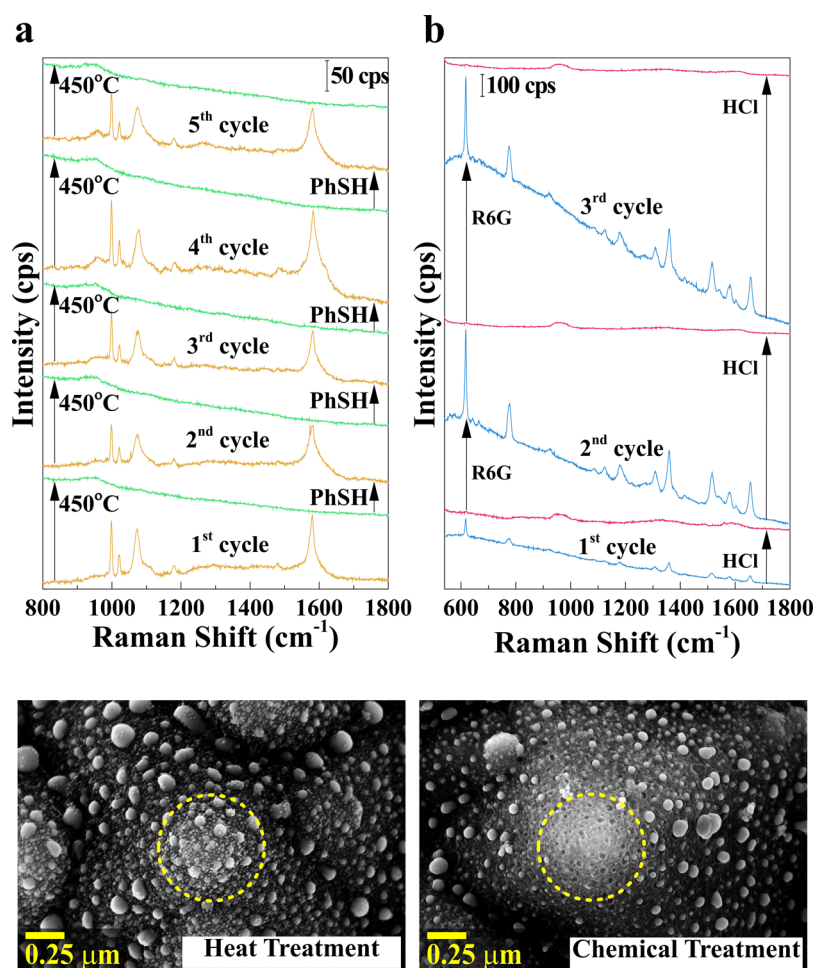
Figure 5. (a) Reusability of the sensor through heat treatment for five cycles, where red and blue represent SERS spectra after drop coating and heating up to 450 °C in air, respectively. FESEM micrograph of heat treated (five cycles) sample depicting its effect on the distribution of AgNPs (secondary growth). (b) Reusability of the sensor through chemical treatment for three cycles, where red and blue represent SERS spectra after drop coating and HCl wash for 5 min, respectively. FESEM micrograph of chemically treated (three cycles) sensor with leaching of AgNPs.

surface area for SERS enhancement. The possibility of detecting fluorescence molecules like R6G, which are used for tagging biological molecules (fluorometric detection), was also demonstrated by our NCES-SERS sensor (Figure 6a).[36,51] To test the SERS detection limit of the NCES-SERS sensor, SERS spectra of PhSH and R6G were acquired for ultralow concentrations (Figure 6b). Up to 10^{-12} M concentrations we were able to detect both the analytes with all their characteristic peaks.

The unique microstructure of etched Si and the AgNP distribution of our NCES-SERS sensor provides interesting prospects for observation of distinctive plasmonic behavior due to the light trapping phenomenon.[18,21,30] To understand the plasmonic behavior of the NCES-SERS sensor, we have performed 2D finite difference time domain (FDTD) simulations. From these simulations, the near field intensity (|E|^2) obtained can be directly correlated to G ($\propto$|E|^4).[11] The size and shape of the AgNPs and size of the micropyramid as well as spacing between the two NPs are found to vary for our NCES-SERS sensor. Therefore, these parameters were modeled individually to study their effects on the near field intensities as their realistic modeling is a challenging task.[52] Figure 7 gives the model with the simulation parameters for the nanocermets on etched and the plain Si SERS sensors designed under identical conditions.

The FDTD near field intensity color plots in Figure 7a, b, d, and e correspond to the parameters: NP size, d = 50 nm, pyramid size, P = 5 μm, and spacing S = 75 nm, based upon the average values from the FESEM data of the NCES-SERS sensor. The hot spot distribution is more clearly visible in the magnified regions W1 and W2 (Figure 7b and e). From these simulation results the distribution of |E|^2 was calculated based upon their number of occurrences in the simulation area and are given in Figure 7c and f, for etched and plain sensors, respectively. The total number of occurrences was significantly more for the etched Si than the plain Si because of larger simulation area involved. Therefore, the near field intensity distribution for higher values was magnified and the data is shown adjacent to the corresponding distributions. The occurrence of higher field intensities is more prominent for the etched sensor, which leads to more enhancement in the SERS signal than the plain sensor. The simulation parameters were also varied individually to study their influence on the near field intensities, the details of which are provided in Supporting Figure S10−S13 and Supporting Videos S1−S3. From these results, it can be inferred that the optimum NP size should be in the range of 50−100 nm, which is also consistent with the experimentally determined NP size (Figure 2 and 3). Furthermore, the simulation predicts that smaller pyramids (P = 1−5 μm) lead to more number of hot spots due to multiple
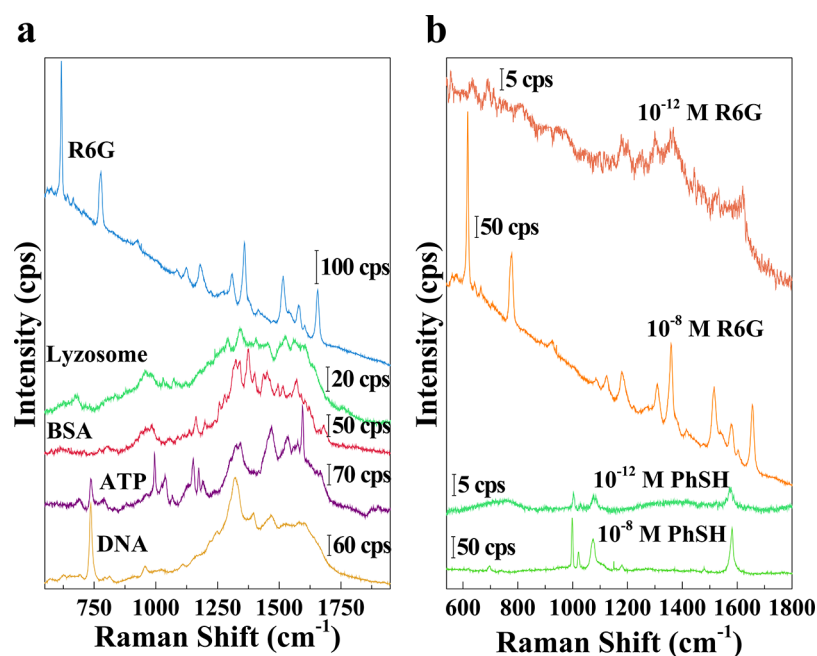
Peak Assignment*

PhSH	1567 cm^{-1}	C-C stretching
R6G	1364-1664 cm^{-1}	C-C (Xanthine ring) stretching
ATP	1334 cm^{-1}	Adenine
DNA	1328 cm^{-1}	Adenine
Lysozyme	1348 cm^{-1}	Tryptophan
BSA	1327-1375 cm^{-1}	Tryptophan

*Detailed assignments are provided in Supporting Information.

Figure 6. (a) SERS spectra of different biomolecules. Main peak assignments are given for each analyte used. Detailed assignments are provided in the Supporting Information. (b) Demonstration of high sensitivity by low (10^{-8} M) and ultralow (10^{-12} M) concentration of PhSH and R6G.
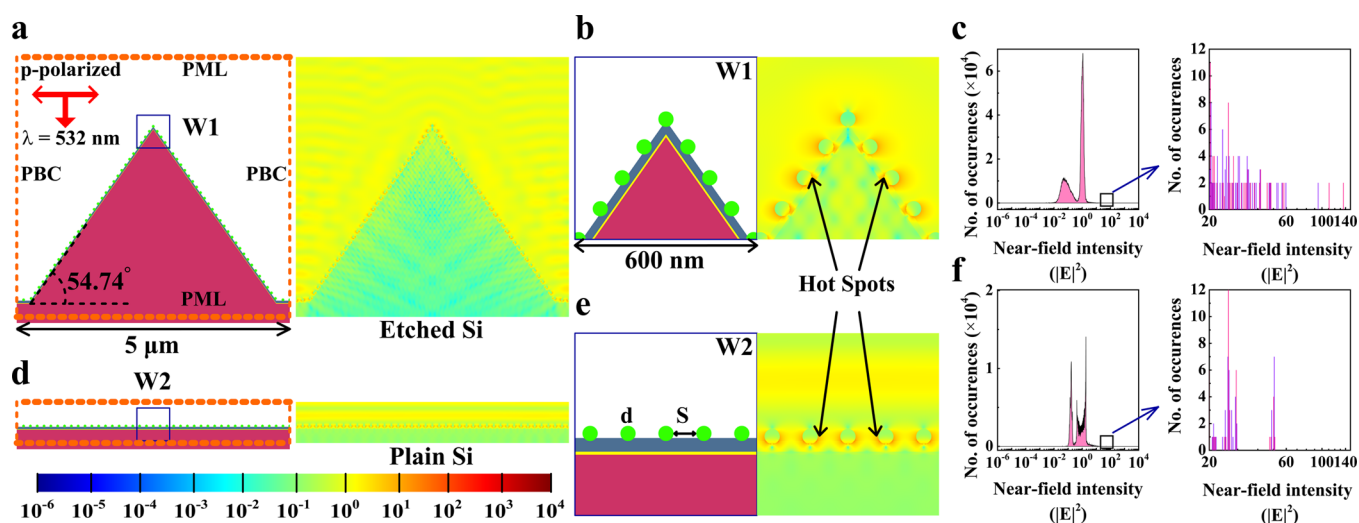

Figure 7. (a) Schematic representation of the 2D FDTD simulation model used to simulate the conditions for the etched Si sensor and the corresponding FDTD field intensity plot. (b) Magnified view of the simulation model (shown as W1 in part a) and the corresponding view of the FDTD field intensity for the etched Si sensor model. (c) Near-field intensity distribution for the etched Si sensor model and a magnified view for the higher intensities (hot spots). For a comparison, parts d–f give the corresponding results for plain Si sensors as parts a–c, respectively. The color bar at the bottom gives the near-field intensity values. For a detailed description of simulation parameters, refer to the Supporting Information.

reflection of the electromagnetic radiation. Also, if NPs are very closely spaced, the near field intensities are very strong, which leads to stronger plasmonic coupling.[53] Additionally, the simulations indicate that among the materials used in the model, Si$_3$N$_4$ and Al$_2$O$_3$ yielded relatively higher near-field intensities than SiO$_2$, presumably because of their higher

refractive indices at 532 nm. Therefore, from the simulation results the distribution of the near-field intensities and the locations of the hot spots, can be linked to the characteristics of the real NCES-SERS sensor in understanding its plasmonic behavior.

An overview of the multifunctionality of our NCES-SERS sensor is provided in the form of a process flow diagram in Supporting Figure S14. Since, the fabrication processes (viz, anisotropic etching of Si and sputtering) involve nonlithographic steps and have a good degree of reproducibility, they can be scaled up easily, and at low-cost for the mass production of the sensor. The presence of a-Si$_3$N$_4$ helps in anchoring and stabilization of AgNPs,[31,54,55] which leads to robustness of the sensor, in terms of chemical and thermal stability. This enables us to use the sensor numerous times for multiple analytes, without any significant degradation in its plasmonic behavior. The unique micro-/nanostructure of the sensor facilitates the detection of various chemical and biological species at very low concentration levels.

CONCLUSION

We have successfully demonstrated the unmatched capability of our NCES-SERS sensor to provide high enhancement in the SERS signal of various analytes with a very high degree of robustness and reusability, which arises because of the unique micro-/nanostructure of the sensor. It was possible to correlate the plasmonic behavior of the sensor with fairly uniform distribution of the AgNPs on Si micropyramids, which also led to the high enhancement factors (e.g., 10^6–10^7 for PhSH) as also substantiated by the 2D FDTD simulations. We have shown that our sensor can work up to 500 °C in air, which can be used to detect very low concentration of analytes that are obtained at high process temperatures. Due to the bare and neutral nature of the AgNPs (no capping agents), the charged analyte molecules (e.g., lysozyme and BSA) do not face any repulsion and are directly accessible to the NP surface, thus facilitating the detection of complex biomolecules such as DNA and proteins. Based upon the FDTD simulation results, we believe that the process parameters for the fabrication of NCES-SERS sensor can be further fine-tuned to obtain very high sensitivity capable of detecting ≤10^{-15} M concentration levels.

ASSOCIATED CONTENT

ⓈSupporting Information

Additional information about NCES-SERS sensors like anisotropic etching of Si, effect of pyramidal structure on the nucleation and growth of Ag thin films, O 1s XPS spectra of NCES-SERS sensors, NP size distribution analysis, SERS enhancement factor calculation, temperature dependent SERS, FDTD analysis, and detailed SERS peak assignments are provided. Three supporting videos are also available for the FDTD simulations of the NCES-SERS sensors. This material is available free of charge via the Internet at http://pubs.acs.org/.

AUTHOR INFORMATION

Corresponding Author
*E-mail: harish@nal.res.in. Phone: +91 80 2508 6494. Fax: +91 80 2521 0113.

Author Contributions
All the authors contributed equally in the development of this manuscript.

REFERENCES

(1) Hazra, S.; Gibaud, A.; Sella, C. Tunable Absorption of Au-Al$_2$O$_3$ Nanocermet Thin Films and its Morphology. *Appl. Phys. Lett.* **2004**, *85*, 395−397.

(2) Toudert, J.; Camelio, S.; Babonneau, D.; Denanot, M.-F.; Girardeau, T.; Espinos, J.; Yubero, F.; Gonzalez-Elipe, A. Morphology and Surface-Plasmon Resonance of Silver Nanoparticles Sandwiched Between Si3N4 and BN Layers. *J. Appl. Phys.* **2005**, *98*, 114316.

(3) Cho, S.; Lee, S.; Lee, T. S.; Cheong, B.-k.; Kim, W. M.; Lee, K.-S. Microstructural Effect on Optical Properties of Au: SiO 2 Nanocomposite Waveguide Films. *J. Appl. Phys.* **2007**, *102*, 123501−123501.

(4) Okumu, J.; Dahmen, C.; Sprafke, A.; Luysberg, M.; Von Plessen, G.; Wuttig, M. Photochromic Silver Nanoparticles Fabricated by Sputter Deposition. *J. Appl. Phys.* **2005**, *97*, 094305.

(5) Klar, T.; Perner, M.; Grosse, S.; von Plessen, G.; Spirkl, W.; Feldmann, J. Surface-Plasmon Resonances in Single Metallic Nanoparticles. *Phys. Rev. Lett.* **1998**, *80*, 4249−4252.

(6) Hutter, E.; Fendler, J. H. Exploitation of Localized Surface Plasmon Resonance. *Adv. Mater.* **2004**, *16*, 1685−1706.

(7) Anker, J. N.; Hall, W. P.; Lyandres, O.; Shah, N. C.; Zhao, J.; Duyne, R. P. V. Biosensing with Plasmonic Nanosensors. *Nat. Mater.* **2008**, *7*, 442−453.

(8) Luther, J. M.; Jain, P. K.; Ewers, T.; Alivisatos, A. P. Localized Surface Plasmon Resonances Arising from Free Carriers in Doped Quantum Dots. *Nat. Mater.* **2011**, *10*, 361−366.

(9) Fan, J. A.; Wu, C.; Bao, K.; Bao, J.; Bardhan, R.; Halas, N. J.; Manoharan, V. N.; Nordlander, P.; Shvets, G.; Capasso, F. Self-Assembled Plasmonic Nanoparticle Clusters. *Science* **2010**, *328*, 1135−1138.

(10) Peng, S.; McMahon, J. M.; Schatz, G. C.; Gray, S. K.; Sun, Y. Reversing the Size-Dependence of Surface Plasmon Resonances. *Proc. Natl. Acad. Sci. U.S.A.* **2010**, *107*, 14530−14534.

(11) Kneipp, K.; Wang, Y.; Kneipp, H.; Perelman, L. T.; Itzkan, I.; Dasari, R. R.; Feld, M. S. Single Molecule Detection Using Surface Enhanced Raman Spectroscopy. *Phys. Rev. Lett.* **1997**, *78*, 1667−1670.

(12) Nie, S.; Emory, S. R. Probing Single Molecules and Single Nanoparticles by Surface-Enhanced Raman Scattering. *Science* **1997**, *275*, 1102−1106.

(13) Lu, Y.; Liu, G. L.; Lee, L. P. High Density Silver Nanoparticle Film with Temperature-Controllable Interparticle Spacing for a Tunable Surface Enhanced Raman Scattering Substrate. *Nano Lett.* **2005**, *5*, 5−9.

(14) Sherry, L. J.; Chang, S.-H.; Schatz, G. C.; Van Duyne, R. P.; Wiley, B. J.; Xia, Y. Localized Surface Plasmon Resonance Spectroscopy of Single Silver Nanocubes. *Nano Lett.* **2005**, *5*, 2034−2038.

(15) Osberg, K. D.; Rycenga, M.; Bourret, G. R.; Brown, K. A.; Mirkin, C. A. Dispersible Surface-Enhanced Raman Scattering Nanosheets. *Adv. Mater.* **2012**, *24*, 6065−6070.

(16) Juve, V.; Cardinal, M. F.; Lombardi, A.; Crut, A.; Maioli, P.; Perez-Juste, J.; Liz-Marzan, L. M.; Fatti, N. D.; Vallee, F. Size-Dependent Surface Plasmon Resonance Broadening in Nonspherical Nanoparticles: Single Gold Nanorods. *Nano Lett.* **2013**, *13*, 2234−2240.

(17) Lim, D.-K.; Jeon, K.-S.; Kim, H. M.; Nam, J.-M.; Suh, Y. D. Nanogap-Engineerable Raman-Active Nanodumbbells for Single-Molecule Detection. *Nat. Mater.* **2010**, *9*, 60−67.

(18) Hu, Y. S.; Jeon, J.; Seok, T. J.; Lee, S.; Hafner, J. H.; Drezek, R. A.; Choo, H. Enhanced Raman Scattering from Nanoparticle-Decorated Nanocone Substrates: A Practical Approach to Harness In-Plane Excitation. *ACS Nano* **2010**, *4*, 5721–5730.

(19) Lee, S. J.; Baik, J. M.; Moskovits, M. Polarization-Dependent Surface-Enhanced Raman Scattering from a Silver-Nanoparticle-Decorated Single Silver Nanowire. *Nano Lett.* **2008**, *8*, 3244–3247.

(20) Chen, T. T.; Kuo, C. S.; Chou, Y. C.; Liang, N. T. Surface-Enhanced Raman Scattering of Adenosine Triphosphate Molecules. *Langmuir* **1989**, *5*, 887–891.

(21) Liang, H.; Li, Z.; Wang, W.; Wu, Y.; Xu, H. Highly Surface-roughened "Flower-like" silver Nanoparticles for Extremely Sensitive Substrates of Surface-enhanced Raman Scattering. *Adv. Mater.* **2009**, *21*, 4614–4618.

(22) Angelis, F. D.; Gentile, F.; Mecarini, F.; Das, G.; Moretti, M.; Candeloro, P.; Coluccio, M. L.; Cojoc, G.; Accardo, A.; Liberale, C.; Zaccaria, R. P.; Perozziello, G.; Tirinato, L.; Toma, A.; Cuda, G.; Cingolani, R.; Fabrizio, E. D. Breaking the Diffusion Limit with Super-hydrophobic Delivery of Molecules to Plasmonic Nanofocusing SERS Structures. *Nat. Photonics* **2011**, *5*, 682–687.

(23) Piorek, B. D.; Lee, S. J.; Santiago, J. G.; Moskovits, M.; Banerjee, S.; Meinhart, C. D. Free-surface Microfluidic Control of Surface-Enhanced Raman Spectroscopy for the Optimized Detection of Airborne Molecules. *Proc. Natl. Acad. Sci. U.S.A.* **2007**, *104*, 18898–18901.

(24) Jeong, E.; Kim, K.; Choi, I.; Jeong, S.; Park, Y.; Lee, H.; Kim, S. H.; Lee, L. P.; Choi, Y.; Kang, T. Three-Dimensional Reduced-Symmetry of Colloidal Plasmonic Nanoparticles. *Nano Lett.* **2012**, *12*, 2436–2440.

(25) Svedberg, F.; Li, Z.; Xu, H.; Käll, M. Creating Hot Nanoparticle Pairs for Surface-Enhanced Raman Spectroscopy through Optical Manipulation. *Nano Lett.* **2006**, *6*, 2639–2641.

(26) Abu Hatab, N.; Oran, J.; Sepaniak, M. Surface-Enhanced Raman Spectroscopy Substrates Created via Electron Beam Lithography and Nanotransfer Printing. *ACS Nano* **2008**, *2*, 377–385.

(27) Fernández-López, C.; Mateo-Mateo, C.; Alvarez-Puebla, R. A.; Pérez-Juste, J.; Pastoriza-Santos, I.; Liz-Marzán, L. M. Highly Controlled Silica Coating of PEG-Capped Metal Nanoparticles and Preparation of SERS-Encoded Particles. *Langmuir* **2009**, *25*, 13894–13899.

(28) Polavarapu, L.; Manga, K. K.; Yu, K.; Ang, P. K.; Cao, H. D.; Balapanuru, J.; Loh, K. P.; Xu, Q.-H. Alkylamine Capped Metal Nanoparticle "Inks" for Printable SERS Substrates, Electronics and Broadband Photodetectors. *Nanoscale* **2011**, *3*, 2268–2274.

(29) Jin, M.; He, G.; Zhang, H.; Zeng, J.; Xie, Z.; Xia, Y. Shape-Controlled Synthesis of Copper Nanocrystals in an Aqueous Solution with Glucose as a Reducing Agent and Hexadecylamine as a Capping Agent. *Angew. Chem., Int. Ed.* **2011**, *50*, 10560–10564.

(30) Cheng, H.-H.; Chang, Y.-Y.; Chu, J.-Y.; Lin, D.-Z.; Chen, Y.-P.; Li, J.-H. Light Trapping Enhancements of Inverted Pyramidal Structures with the Tips for Silicon Solar Cells. *Appl. Phys. Lett.* **2012**, *101*, 141113.

(31) Baraldi, G.; Carrada, M.; Toudert, J.; Ferrer, F. J.; Arbouet, A.; Paillard, V.; Gonzalo, J. Preventing the Degradation of Ag Nano-particles Using an Ultrathin a-Al2O3 Layer as Protective Barrier. *J. Phys. Chem. C* **2013**, *117*, 9431–9439.

(32) Garcia, S. P.; Bao, H.; Hines, M. A. Etchant Anisotropy Controls the Step Bunching Instability in KOH Etching of Silicon. *Phys. Rev. Lett.* **2004**, *93*, 166102.

(33) Brune, H. Microscopic View of Epitaxial Metal Growth: Nucleation and Aggregation. *Surf. Sci. Rep.* **1998**, *31*, 121–129.

(34) Kudelski, A. Raman Studies of Rhodamine 6G and Crystal Violet Sub-Monolayers on Electrochemically Roughened Silver Substrates: Do Dye Molecules Adsorb Preferentially on Highly SERS-Active Sites? *Chem. Phys. Lett.* **2005**, *414*, 271–275.

(35) Peng, P.; Ling, K.-J.; Tse, W. S. SERS of Crystal Violet in Sandblast Roughened Silver Surface. *Mod. Phys. Lett. B* **1990**, *04*, 531–534.

(36) Smith, C. Keeping Tabs on Fluorescent Tags. *Nat. Methods* **2007**, *4*, 755–762.

(37) Bao, X.; Muhler, M.; Schedel-Niedrig, T.; Schlögl, R. Interaction of Oxygen with Silver at High Temperature and Atmospheric Pressure: A Spectroscopic and Structural Analysis of a Strongly Bound Surface Species. *Phys. Rev. B* **1996**, *54*, 2249–2262.

(38) Bi, H.; Cai, W.; Kan, C.; Zhang, L.; Martin, D.; Träger, F. Optical Study of Redox Process of Ag Nanoparticles at High Temperature. *J. Appl. Phys.* **2002**, *92*, 7491–7497.

(39) Balamurugan, B.; Maruyama, T. Evidence of an Enhanced Interband Absorption in Au Nanoparticles: Size-Dependent Electronic Structure and Optical Properties. *Appl. Phys. Lett.* **2005**, *87*, 143105–143105.

(40) Thornton, J. A. High Rate Thick Film Growth. *Annu. Rev. Mater. Sci.* **1977**, *7*, 239–260.

(41) Jain, P. K.; Huang, X.; El-Sayed, I. H.; El-Sayed, M. A. Noble Metals on the Nanoscale: Optical and Photothermal Properties and Some Applications in Imaging, Sensing, Biology, and Medicine. *Acc. Chem. Res.* **2008**, *41*, 1578–1586.

(42) Kelly, K. L.; Coronado, E.; Zhao, L. L.; Schatz, G. C. The Optical Properties of Metal Nanoparticles: The Influence of Size, Shape, and Dielectric Environment. *J. Phys. Chem. B* **2003**, *107*, 668–677.

(43) Stiles, P. L.; Dieringer, J. A.; Shah, N. C.; Van Duyne, R. P. Surface-Enhanced Raman Spectroscopy. *Annu. Rev. Anal. Chem.* **2008**, *1*, 601–626.

(44) Kneipp, K.; Kneipp, H.; Abdali, S.; Berg, R. W.; Bohr, H. Single Molecule Raman Detection of Enkephalin on Silver Colloidal Particles. *J. Spectrosc.* **2004**, *18*, 433–440.

(45) Le Ru, E. C.; Meyer, S. A.; Artur, C.; Etchegoin, P. G.; Grand, J.; Lang, P.; Maurel, F. Experimental Demonstration of Surface Selection Rules for SERS on Flat Metallic Surfaces. *Chem. Commun.* **2011**, *47*, 3903–3905.

(46) Yeng, Y. X.; Ghebrebrhan, M.; Bermel, P.; Joannopoulos, W. R. C. J. D.; Solijacic, M.; Celanovic, I. Enabling High-Temperature Nanophotonics for Energy Applications. *Proc. Natl. Acad. Sci. U.S.A.* **2012**, *109*, 2280–2285.

(47) Liu, J.-W.; Wang, J.-L.; Huang, W.-R.; Yu, L.; Ren, X.-F.; Wen, W.-C.; Yu, S.-H. Ordering Ag Nanowire Arrays by a Glass Capillary: A Portable, Reusable and Durable SERS Substrate. *Sci. Rep.* **2012**, *2*, 1–6.

(48) Kang, T.; Yoo, S. M.; Yoon, I.; Lee, S. Y.; Kim, B. Patterned Multiplex Pathogen DNA Detection by Au Particle-on-Wire SERS Sensor. *Nano Lett.* **2010**, *10*, 1189–1193.

(49) von Maltzahn, G.; Centrone, A.; Park, J.-H.; Ramanathan, R.; Sailor, M. J.; Hatton, T. A.; Bhatia, S. N. SERS-Coded Gold Nanorods as a Multifunctional Platform for Densely Multiplexed Near-Infrared Imaging and Photothermal Heating. *Adv. Mater.* **2009**, *21*, 3175–3180.

(50) Lee, S.; Chon, H.; Yoon, S.-Y.; Lee, E. K.; Chang, S.-I.; Lim, D. W.; Choo, J. Fabrication of SERS-Fluorescence Dual Modal Nanoprobes and Application to Multiplex Cancer Cell Imaging. *Nanoscale* **2012**, *4*, 124–129.

(51) Romanini, D. W.; Cornish, V. W. Protein Labelling: Playing Tag with Proteins. *Nat. Chem.* **2012**, *4*, 248–250.

(52) Thoreson, M. D.; Fang, J.; Kildishev, A. V.; Prokopeva, L. J.; Nyga, P.; Chettiar, U. K.; Shalaev, V. M.; Drachev, V. P. Fabrication and Realistic Modeling of Three-Dimensional Metal-Dielectric Composites. *J. Nanophotonics* **2011**, *5*, 051513–051513.

(53) Su, K.-H.; Wei, Q.-H.; Zhang, X.; Mock, J.; Smith, D. R.; Schultz, S. Interparticle Coupling Effects on Plasmon Resonances of Nanogold Particles. *Nano Lett.* **2003**, *3*, 1087–1090.

(54) Zhang, X.; Zhao, J.; Whitney, A. V.; Elam, J. W.; Van Duyne, R. P. Ultrastable Substrates for surface-Enhanced Raman Spectroscopy: Al2O3 Overlayers Fabricated by Atomic Layer Deposition Yield Improved Anthrax Biomarker Detection. *J. Am. Chem. Soc.* **2006**, *128*, 10304–10309.

(55) Uzayisenga, V.; Lin, X.-D.; Li, L.-M.; Anema, J. R.; Yang, Z.-L.; Huang, Y.-F.; Lin, H.-X.; Li, S.-B.; Li, j.-F.; Tian, Z.-Q. Synthesis, Characterization, and 3D-FDTD Simulation of Ag@SiO2 Nano-

particles for Shell-Isolated Nanoparticle-Enhanced Raman Spectroscopy. *Langmuir* **2012**, *28*, 9140−9146.